J. Hydrol. Hydromech., 73, 2025, 2, 155–174
https://doi.org/10.2478/johh-2025-0012

sciendo Journal of Hydrology and Hydromechanics Institute of Hydrology SAS

Highly concentrated iron ore slurry flow through pipeline with and without chemical additive; part II: 3d cfd modelling

Stuti Mishra*, Deo Raj Kaushal

Department of Civil Engineering, Indian Institute of Technology Delhi, Hauz Khas, New Delhi 110016, India.
* Corresponding author. E-mail: stuti.mishra@civil.iitd.ac.in

Abstract: This study involves a computational analysis of the flow of iron ore (with a mean particle diameter of 55 microns) slurry flow through a pipeline of 2-inch diameter. The analysis covers a flow velocity range of 1 to 3.5 m/s at high concentrations ranging from 60 to 72 % w/w without and with additive (Sodium-hexametaphosphate) at different dosages from 0.1 to 1.5% w/w of solids. A three-dimensional Computational Fluid Dynamics (3D CFD) model is developed and validated using experimental data collected in our previous studies (Part I). The Eulerian multiphase model is used with K-epsilon turbulence settings to simulate the flow. Based on comparison with experimental data, it is observed that the 3D CFD model can predict the pressure drop with an error band of ±30%. However, the 3D CFD model predicts the pressure drop very accurately for the velocity range of 2 to 3m/s for the entire range of solids concentrations considered in the present study. Distributions of concentration, velocity, and slip velocity along with granular pressure and granular viscosity are also computed and presented using the 3D CFD model developed in the present study for the entire ranges of solids concentration and flow velocity covered in the present study.

Keywords: Iron ore; Slurry flow; CFD.

1 INTRODUCTION

Pipeline transportation of industrial powder/granular materials have long been used over the decades and is mostly used in thermal power, pharmaceuticals industry, mineral industry, and others. It is one of the most economical and environmentally friendly transportation. Slurry pipelines are recognized for their minimal maintenance needs, which vary based on usage, year-round availability, and environmental considerations. As closed conduits, slurry pipelines are regarded by numerous industries as a vital method for transporting solids both within and outside of production facilities. In thermal power plants, slurry pipelines are employed for the transportation of iron ore, fly ash, and bed ash for various applications, as well as to convey tailings to mine dumps.

Research on multi-sized particle slurries has primarily concentrated on the transport properties and interactions among particles of different sizes, which significantly influence pressure drops during pipeline conveyance. Below a certain velocity, the particles may settle, causing the slurry to behave either as a Newtonian or non-Newtonian fluid. The corrosiveness and abrasiveness of the slurry can vary based on its composition. The complex issues of predicting pressure drops and flow patterns are largely addressed through correlations derived from experimental data.

Since a slurry contains two mediums, i.e., water as the primary phase and particles as the secondary phase, the computational analysis of slurry flows is termed multiphase modeling. When large or heavy particles are added to a slurry, the system must then be treated as a multiphase flow system because heavy particles tend to segregate very rapidly. In such systems, fluidization is used to obtain good mixing and avoid particles settling under their weight. Various factors are involved in the in-situ operation of slurry pipeline flow and modeling them computationally needs a lot of preciseness. Thus, it is important to validate the ability of current models to simulate the mixing of multiphase flow systems involving Newtonian and non-Newtonian fluids.

Computational Fluid Dynamics evolved to be an effective tool for complex flow modeling as multiphase flow in the pipeline as it offers greater flexibility and ease to tackle an unlimited number of physical and operating conditions (Singh et al. 2024). Several studies have been conducted where CFD-based models are used to simulate the pipeline flows. Kumar et al (2019) considered a higher solid concentration of iron ore slurry and conducted experimental as well as CFD analysis having particles of the very fine size of 12 microns. Although a wide velocity range was tested with varied concentrations, rheological testing was missing from the work which gives an actual idea about the behavior of slurry inside the pipeline majorly consisting of the viscosity and yield stress properties. Avksentiev et al. (2017) conducted a comparative examination of various techniques employed for predicting pressure drop based on rheological data. The computed outcomes indicated that analytical relationships for determining pressure loss and hydraulic resistance coefficient can be applicable in the analysis of non-Newtonian fluids and loss determination. The models considered encompass viscous fluids characterized by initial shear stress as the concentration of the solid phase in the iron ore hydraulic fluid increases, and they also incorporated the effective dynamic viscosity as demonstrated by the Bingham-Shvedov model. Das et al. (2020) have reported stabilizing several slurries with their rheological behavior and CFD study for practical pipeline transportation, notably iron ore slurry. Their work is surrounded by the comparative analysis of different works carried out and suggests that pipeline is a better mode for transportation of slurry rather than roads and railways.

Even though the experimental and rheological studies give us a ground reality of pipeline slurry transportation, the coputational analysis by modeling the flow helps us in predicting the pressure drop without wasting much of the material and resources by conducting experiments for each and every case consideration. Kumar et al. (2017) did a study on the horizontal slurry flow (water-glass beads) of smaller particles via a pipeline and computationally simulated it in their research. Through a 54.9 mm diameter pipe, a slurry consisting of glass beads with water having 125 µm mean diameter particles is examined at concentrations up to 50% while running at varied flow velocities up to 5 m/s and investigated the monodispersed glass bead particles with a density of 2470 kg/m3 using an Eulerian model with RNG k-turbulence model.

Hernández et al. (2008) focused on using the Eulerian-Eulerian method to describe the movement of sand particles and water in a horizontal conduit. They have addressed both heterogeneous and homogeneous flow patterns. The turbulent effects were modeled using the k epsilon model. Solid-phase stress description is also very important for the completion of solid-phase momentum equations. The results demonstrate that the pseudo-viscosity and restitution coefficient of the solid phase have a significant impact on flow predictions. Additionally, compared to findings produced using other computational models, these simulated results were more similar to experimental data giving an affirmation that CFD results can give closer findings to the experimental data. Kumar et al. (2019) made an effort to experimentally investigate and create a CFD-based model for a highly concentrated iron ore slurry through a 105mm diameter pipeline. The mean particle size was 12 µm with an efflux concentration range of 2.63 – 31%. The simulated results were quite encouraging when compared with the pipe loop tests, however effect of additive or change in yield stress/viscous properties was yet to be seen in the CFD results.

After going through the literature already done in the past, it has been found that there is an insufficient study about the high concentration of iron ore slurry for a 3D CFD–based model. To reduce the material and resource usage for conducting experiments in each case, the development of a computational model for the same slurry becomes essential to predict the pressure drop across the pipeline at various concentrations and velocities. So, in this study, CFD simulations and their results are discussed thoroughly for iron ore slurry in a pipeline, with and without chemical additive. The rheological model and experimental studies already done by Mishra and Kaushal (2025) in the Part I studies are taken as initial points for simulating the CFD model. A 3D CFD–based model has been created and verified using the outcomes of the pipe loop experiments for pressure drop. Furthermore, slip velocity is of utmost importance for determining the slurry's stability, hence in this study, the slip velocity of iron ore slurry is also studied thoroughly in the vertical as well as horizontal direction of the pipeline using the 3D CFD–based model.

2 METHODOLOGY

2.1 3D CFD-based model

FLUENT describes the flow behaviour of a fluid-solid combination using a multi–fluid granular model. The solid-phase stresses are determined by making a comparison between the random particle motion caused by particle-particle collisions. Ansys Fluent 2021 is used to simulate the flow. Here, the liquid and solid phases are both seen as being in a continuum according to the Eulerian-Eulerian two-fluid paradigm. By solving the momentum and continuity equations for each phase, this method makes it possible to identify the specific flow field solutions. The most intricate and computationally demanding of the multiphase models is the Eulerian model. It resolves a set of momentum and continuity equations for "n" numbers for every phase. A pressure-interphase exchange coefficient relationship is seen. Application of the kinetic theory yields the characteristics of granular flows. The particulars of the sole model that yielded the converged outcomes are presented hereafter.

Various forces are exerted on an individual particle within a fluid. (Kaushal et al., 2012):

1. Static pressure gradient, ∇P.
2. The gradient in solid pressure, alternatively referred to as the inertial force arising from particle interactions., ∇P_s.
3. The drag force induced by disparities in velocity between two phases, $K_{sf}(\vec{v}_s - \vec{v}_f)$, where, K_{sf} is the inter-phase drag coefficient, $\vec{v}_s$ and $\vec{v}_f$ are velocity of the solid and fluid phase.
4. Viscous forces, $\nabla \cdot \bar{\bar{\tau}}_f$, where, $\bar{\bar{\tau}}_f$ is the stress tensor for fluid.
5. Body forces, $\rho\vec{g}$ where ρ is the density and g is the acceleration due to gravity.
6. Virtual mass force, $C_{vm}\alpha_s\rho_f(\vec{v}_f \cdot \nabla\vec{v}_f - \vec{v}_s \cdot \nabla\vec{v}_s)$, where, C_{vm} is the coefficient of virtual mass force.
7. Lift force, where, $C_L\alpha_s\rho_f(\vec{v}_f - \vec{v}_s) \times (\nabla \times \vec{v}_f)$ where, C_L is the lift coefficient.

2.1.1 Governing equations

The solution to the continuity equation for the volume fraction of one (or more) of the phases enables the monitoring of the interface(s) between the phases and is expressed as follows:

$$\nabla \cdot (\alpha_t\rho_t\vec{v}_t) = 0 \tag{1}$$

where the t represents solid(s) or fluid (f).

Momentum equations for the fluid phase:

$$\nabla \cdot (\alpha_f\rho_f\vec{v}_f\vec{v}_f) = -\alpha_f\nabla P + \nabla \cdot \bar{\bar{\tau}}_f + \alpha_f\rho_f\vec{g} + K_{sf}(\vec{v}_s - \vec{v}_f) + C_{vm}\alpha_f\rho_f(\vec{v}_s \cdot \nabla\vec{v}_s - \vec{v}_f \cdot \nabla\vec{v}_f) + C_L\alpha_s\rho_f(\vec{v}_f - \vec{v}_s) \times (\nabla \times \vec{v}_f) \tag{2}$$

For the solid phase:

$$\nabla \cdot (\alpha_s\rho_s\vec{v}_s\vec{v}_s) = -\alpha_s\nabla P - \nabla P_s + \nabla \cdot \bar{\bar{\tau}}_s + \alpha_s\rho_f\vec{g} + K_{fs}(\vec{v}_f - \vec{v}_s) + C_{vm}\alpha_s\rho_f(\vec{v}_f \cdot \nabla\vec{v}_f - \vec{v}_s \cdot \nabla\vec{v}_s) + C_L\alpha_s\rho_f(\vec{v}_s - \vec{v}_f) \times (\nabla \times \vec{v}_f) \tag{3}$$

where, $\bar{\bar{\tau}}_f$ is the fluid's stress tensor and $\bar{\bar{\tau}}_s$ is the solid's stress tensor, which is written as:

$$\bar{\bar{\tau}}_f = \alpha_f\mu_f(\nabla\vec{v}_f + \nabla\vec{v}_f^{\,tr}) \tag{4}$$

and

$$\bar{\bar{\tau}}_s = \alpha_s\mu_s(\nabla\vec{v}_s + \nabla\vec{v}_s^{\,tr}) + \alpha_s(\lambda_s - \tfrac{2}{3}\mu_s)\nabla \cdot \vec{v}_s\bar{\bar{I}} \tag{5}$$

where the superscript 'tr' over the velocity vector indicates transpose. $\bar{\bar{I}}$ is the identity tensor. λ_s is the bulk viscosity of the solids as given by:

$$\lambda_s = \tfrac{4}{3}\alpha_s\rho_s d_s g_{0,ss}(1 + e_{ss})(\tfrac{\theta_s}{\pi})^{\frac{1}{2}} \tag{6}$$

where the diameter of the particle is $\boldsymbol{d_s}$ as 55µm. $\boldsymbol{g_{0,ss}}$ is the function of radial distribution, construed as the likelihood of a particle contacting the other particle, is expressed as:

$$\boldsymbol{g_{0,ss}} = \left[\mathbf{1} - \left(\frac{\alpha_s}{\alpha_{s,max}}\right)^{\frac{1}{3}}\right]^{-\mathbf{1}} \quad (7)$$

$\boldsymbol{\alpha_{s,max}}$ is the experimentally measured iron ore slurry's static settled concentration as 0.36. Θ*s* represents the granular temperature, a quantity directly proportional to the kinetic energy associated with the fluctuating movement of particles. *ess* denotes the restitution coefficient, assigned a value of 0.9 for iron ore particles. *µf* stands for the shear viscosity of the fluid, while *µs* corresponds to the shear viscosity of the solid and is expressed as:

$$\boldsymbol{\mu_s} = \boldsymbol{\mu_{s,col}} + \boldsymbol{\mu_{s,kin}} + \boldsymbol{\mu_{s,fr}} \quad (8)$$

where, $\boldsymbol{\mu_{s,col}}$ is the collisional viscosity, $\boldsymbol{\mu_{s,fr}}$ is the frictional viscosity, and $\boldsymbol{\mu_{s,kin}}$ is the kinetic viscosity. The following equations is used to calculate them.

$$\boldsymbol{\mu_{s,col}} = \frac{\mathbf{4}}{\mathbf{3}}\boldsymbol{\alpha_s \rho_s d_s g_{0,ss}}(\mathbf{1} + \boldsymbol{e_{ss}})\left(\frac{\boldsymbol{\Theta_s}}{\boldsymbol{\pi}}\right)^{\frac{1}{2}} \quad (9)$$

$$\boldsymbol{\mu_{s,fr}} = \frac{\boldsymbol{P_s sin\phi}}{\mathbf{2}\sqrt{\boldsymbol{I_{2D}}}} \quad (10)$$

and

$$\boldsymbol{\mu_{s,kin}} = \frac{\alpha_s d_s \rho_s \sqrt{\Theta_s \pi}}{6(3-e_{ss})}\left[\mathbf{1} + \frac{\mathbf{2}}{\mathbf{5}}(\mathbf{1} + \boldsymbol{e_{ss}})(\mathbf{3}\boldsymbol{e_{ss}} - \mathbf{1})\boldsymbol{\alpha_s g_{0,ss}}\right] \quad (11)$$

$\boldsymbol{I_{2D}}$, the solid phase's deviatoric strain rate tensor in its second invariant. The solid pressure (P_s) is given by:

$$\boldsymbol{P_s} = \boldsymbol{\alpha_s \rho_s \Theta_s} + \mathbf{2}\boldsymbol{\rho_s}(\mathbf{1} + \boldsymbol{e_{ss}})\boldsymbol{\alpha_s}^{\mathbf{2}}\boldsymbol{g_{0,ss}\Theta_s} \quad (12)$$

$\boldsymbol{\phi}$ is the angle of internal friction taken as 30°. K_{fs} (=K_{sf}), the interphase coefficient of momentum exchange represented by:

$$\boldsymbol{K_{sf}} = \boldsymbol{K_{fs}} = \frac{\mathbf{3}}{\mathbf{4}}\frac{\boldsymbol{\alpha_s \alpha_f \rho_f}}{\boldsymbol{V_{r,s}^2 d_s}}\boldsymbol{C_D}\left(\frac{\boldsymbol{Re_s}}{\boldsymbol{V_{r,s}}}\right)|\vec{\boldsymbol{v}}_s - \vec{\boldsymbol{v}}_f| \quad (13)$$

Drag coefficient $$\boldsymbol{C_D} = \left[\mathbf{0.63} + \mathbf{4.8}\left(\frac{\boldsymbol{Re_s}}{\boldsymbol{V_{r,s}}}\right)^{-\frac{1}{2}}\right]^{\mathbf{2}} \quad (14)$$

Re_s is the relative Reynolds number between phases 'f' and 's' given by:

$$\boldsymbol{Re_s} = \frac{\boldsymbol{\rho_s d_s}|\vec{\boldsymbol{v}}_s - \vec{\boldsymbol{v}}_f|}{\boldsymbol{\mu_f}} \quad (15)$$

$\boldsymbol{V_{r,s}}$ is the terminal velocity correlation for the phase of solid given by:

$$\boldsymbol{V_{r,s}} = \mathbf{0.5}\Big(\boldsymbol{A} - \mathbf{0.06}\boldsymbol{Re} + \sqrt{(\boldsymbol{Re_s})^{\mathbf{2}} + \mathbf{0.12}\boldsymbol{Re_s}(\mathbf{2}\boldsymbol{B} - \boldsymbol{A}) + \boldsymbol{A}^{\mathbf{2}}}\Big) \quad (16)$$

with

A=$\boldsymbol{\alpha_f^{4.14}}$; $\boldsymbol{B} = \boldsymbol{\alpha_f^{1.28}}$ for $\boldsymbol{\alpha_f} \leq \mathbf{0.85}$, (17)

and

A=$\boldsymbol{\alpha_f^{4.14}}$; $\boldsymbol{B} = \boldsymbol{\alpha_f^{2.65}}$ for $\boldsymbol{\alpha_f} > \mathbf{0.85}$ (18)

Utilizing the conventional K–ε model involves generating forecasts for the turbulent characteristics within the fluid phase, incorporating supplementary terms to accommodate the transfer of turbulent momentum across interfaces.

The fluid phase's Reynolds stress tensor 'f' is

$$\bar{\bar{\boldsymbol{\tau}}}_{t,f} = -\frac{\mathbf{2}}{\mathbf{3}}(\boldsymbol{\rho_f k_f} + \boldsymbol{\mu_{t,f}}\nabla\vec{\boldsymbol{v}}_f)\bar{\bar{\boldsymbol{I}}} + \boldsymbol{\mu_{t,f}}(\nabla\vec{\boldsymbol{v}}_f + \nabla\vec{\boldsymbol{v}}_f^{\,tr}) \quad (19)$$

where, $\boldsymbol{\mu_{t,f}}$ is the turbulent viscosity given by:

$$\boldsymbol{\mu_{t,f}} = \boldsymbol{\rho_f C_\mu}\frac{k_f^2}{\varepsilon_f} \text{ with } \boldsymbol{C_\mu}\text{=0.09} \quad (20)$$

The prediction of turbulent kinetic energy $\boldsymbol{k_f}$ and its dissipation rate $\boldsymbol{\varepsilon_f}$, are obtained from the following transport equations:

$$\nabla\cdot(\boldsymbol{\alpha_f \rho_f \vec{U}_f k_f}) = \nabla\cdot\left(\boldsymbol{\alpha_f}\frac{\mu_{t,f}}{\sigma_k}\nabla\boldsymbol{k_f}\right) + \boldsymbol{\alpha_f G_{kf}} - \boldsymbol{\alpha_f \rho_f \varepsilon_f} + \boldsymbol{\alpha_f \rho_f \Pi_{kf}} \quad (21)$$

$$\nabla\cdot(\boldsymbol{\alpha_f \rho_f \vec{U}_f k_f}) = \nabla\cdot\left(\boldsymbol{\alpha_f}\frac{\mu_{t,f}}{\sigma_\varepsilon}\nabla\boldsymbol{\varepsilon_f}\right) + \boldsymbol{\alpha_f}\frac{\varepsilon_f}{k_f}(\boldsymbol{C_{1\varepsilon}G_{k,f}} - \boldsymbol{C_{1\varepsilon}\rho_f \varepsilon_f}) + \boldsymbol{\alpha_f \rho_f \Pi_{\varepsilon f}} \quad (22)$$

where $\boldsymbol{\Pi_{kf}}$ and $\boldsymbol{\Pi_{\varepsilon f}}$ represent phase of solid 's' influence onto the phase of fluid 'f' expressed as

$$\boldsymbol{\Pi_{kf}} = \frac{\boldsymbol{k_{sf}}}{\boldsymbol{\alpha_f \rho_f}}(\boldsymbol{k_{sf}} - \mathbf{2}\boldsymbol{k_f} + \vec{\boldsymbol{v}}_{sf}.\vec{\boldsymbol{v}}_{dr}) \quad (23)$$

$$\boldsymbol{\Pi_{\varepsilon f}} = \boldsymbol{C_{3\varepsilon}}\frac{\boldsymbol{\varepsilon_f}}{\boldsymbol{k_f}}\boldsymbol{\Pi_{kf}} \quad (24)$$

$\vec{\boldsymbol{v}}_{dr}$ is the drift velocity given as:

$$\vec{\boldsymbol{v}}_{dr} = \left(\frac{\boldsymbol{D_s}}{\boldsymbol{\alpha_{sf}\alpha_s}}\nabla\boldsymbol{\alpha_s} - \frac{\boldsymbol{\mu_{t,f}}}{\boldsymbol{\alpha_{sf}\alpha_s}}\nabla\boldsymbol{\alpha_f}\right) \quad (25)$$

$\nabla\boldsymbol{\alpha_s}$ in above Eq. (25) considers the fluctuation in concentrations. $\vec{\boldsymbol{v}}_{sf.}$ is the slip-velocity, the relative velocity between the phase of fluid and phase of solid given by:

$$\vec{\boldsymbol{v}}_{sf} = \vec{\boldsymbol{v}}_s - \vec{\boldsymbol{v}}_f \quad (26)$$

$\boldsymbol{D_s}$ = solid sections's eddy viscosity, $\boldsymbol{\alpha_{sf}}$ = constant (0.75), $\boldsymbol{k_{sf}}$ is the average product of the variation in the solid and fluid phase's respective velocities, and it is defined as the covariance of their velocities. The rate at which kinetic energy is extracted from the mean and organized movements by the Reynolds stresses, or $G_{k,f}$, is the creation of flow's turbulent kinetic energy expressed as follows:

$$\boldsymbol{G_{k,f}} = \boldsymbol{\mu_{t,f}}(\nabla\vec{\boldsymbol{v}}_f + \nabla\vec{\boldsymbol{v}}_f^{\,t}) : \nabla\vec{\boldsymbol{v}}_f \quad (27)$$

The different equations constant parameters are written as:

$$\boldsymbol{C_{1\varepsilon}} = \mathbf{1.44}, \boldsymbol{C_{2\varepsilon}} = \mathbf{1.92}, \boldsymbol{C_{3\varepsilon}} = \mathbf{1.2}, \boldsymbol{\sigma_k} = \mathbf{1.0}, \boldsymbol{\sigma_\varepsilon} = \mathbf{1.3} \quad (28)$$

Tchen's theory, as described by Lun et al. in 1984, is employed to forecast turbulence within the solid phase. This theory addresses inhomogeneous and steady turbulent flow for the dispersion of discrete particles. The representation of turbulent kinetic energy, dispersion coefficients, and correlation functions within the solid phase is contingent upon the essential characteristics of the continuous turbulent motion's time scale in the fluid phase and the characteristic time.

$$\tau_{F,sf} = \alpha_s \rho_f K_{sf}^{-1} \left(\frac{\rho_s}{\rho_f} + C_{vm} \right) \tag{29}$$

The characteristic time of the interaction between eddies and particles:

$$\tau_{t,sf} = \tau_{t,f} \left[1 + C_\beta \xi^2 \right]^{\frac{1}{2}} \tag{30}$$

$$\xi = \frac{|\vec{V}_r|}{\sqrt{\frac{2k_f}{3}}} \tag{31}$$

The energetic, turbulent eddies characteristic time:

$$\tau_{t,f} = \frac{3}{2} C_\mu \frac{k_f}{\varepsilon_f} \tag{32}$$

$|\vec{V}_r| = \vec{v}_{sf}$ - $\vec{v}_{dr}$, $|\vec{V}_r|$ being the local relative velocity's average value between particle and fluid known as drift and slip velocity.

$$C_\beta = 1.8 - 1.35 cos^2\theta \tag{33}$$

θ is the particle's mean velocity and mean relative velocity mid-angle and η_{sf} is two characteristic time ratios given as:

$$\eta_{sf} = \frac{\tau_{t,sf}}{\tau_{F,sf}} \tag{34}$$

The solid phase's turbulent kinetic energy,

$$k_s = k_f \left(\frac{b^2 + \eta_{sf}}{1 + \eta_{sf}} \right) \tag{35}$$

Eddy viscosity for the solid phase,

$$D_s = D_{t,sf} + \left(\frac{2}{3} k_s - b \frac{1}{3} k_{sf} \right) \tau_{F,sf} \tag{36}$$

Binary turbulent diffusion coefficient,

$$D_{t,sf} = \frac{1}{3} k_s \tau_{t,sf} \tag{37}$$

where, b= (1+C_{Vm}) $\left(\frac{\rho_s}{\rho_f} + C_{Vm} \right)^{-1}$

The kinetic energy of solid particles undergoing random motion is elucidated by the granular temperature within the solid phase. The governing transport equation, as derived from the kinetic theory proposed by Gidaspow et al. (1992), is expressed as follows:

$$\frac{2}{3} \nabla \cdot (\alpha_s \rho_s \vec{v}_s \Theta_s) = \left(-P_s \bar{\bar{I}} + \bar{\bar{\tau}} s \right) : \nabla \vec{v}_s + \nabla \cdot \left(k_{\Theta_s} \nabla \Theta_s \right) - \gamma_{\Theta_s} + \varphi_s \tag{38}$$

Here, the development of energy from the solid stress tensor is defined by $\left(-P_s \bar{\bar{I}} + \bar{\bar{\tau}} s \right) : \nabla \vec{v}_s$. k_{Θ_s} being the diffusion coefficient given as:

$$k_{\Theta_s} = \frac{15 d_s \rho_s \alpha_s \sqrt{\Theta_s \pi}}{4(41 - 33\eta)} \left[1 + \frac{12}{5} \eta^2 (4\eta - 3) \alpha_s g_{0,ss} + \frac{16}{15\pi} (41 - 33\eta) \eta \alpha_s g_{0,ss} \right] \tag{39}$$

$k_{\Theta_s} \nabla \Theta_s$ is the granular energy's diffusive flux.

$$\eta = \frac{1}{2} (1 + e_{ss}) \tag{40}$$

Collisional dissipation energy,

$$\gamma_{\Theta_s} = \frac{12(1 - e_{ss}{}^2) g_{0,ss}}{d_s \sqrt{\pi}} \rho_s \alpha_s{}^2 \Theta_s{}^{\frac{3}{2}} \tag{41}$$

φ_{fs} is the kinetic energy's transfer due to an unsystematic motion in the velocity of particle from the phase of solid to the phase of fluid and is expressed as:

$$\varphi_{fs} = -3 K_{fs} \Theta_s \tag{42}$$

2.1.2 Mesh

Meshing constitutes a crucial aspect of computational modeling. The model domain, measuring 4.5 meters in length and possessing an internal diameter of 50.8 mm, was generated using the meshing tool in Ansys Fluent 2021. It comprises 2,347,500 elements and 2,431,620 nodes, a determination confirmed through a mesh independency check. The length of the pipeline closely aligns with that of the original experimental setup to ensure comprehensive flow development. The inflation layers exhibit a seamless transition with six layers, aimed at accurately representing the boundary flow. Employing multi-zone meshing with an element order size of 3 x 10^{-3}m and a skewness of 0.90, the mesh was verified to be compatible with the turbulence model, yielding reproducible and converged results.

Figure 1 illustrates the specifics of meshing within the cross-sectional region of the pipeline. Inflation layers have been incorporated to enhance the resolution of the boundary layer and effectively capture wall gradients. Figure 2 provides a depiction of three-dimensional meshing details for the pipeline. Table 1 presents the particulars of the model setup employed in the investigation to simulate the flow of slurry within the pipeline.

Table 1. Model setup details.

Turbulence model	K–epsilon
Time step chosen	Steady–state
Number of time step	Steady–state
Volume fraction formulation	Implicit
Phase interaction	Water iron–ore: drag coefficient schiller-Naumann

2.1.3 Inclusion of Rheological properties into the 3D CFD-based model

The rheological properties of the slurry play a pivotal role in deciding the type of model needed to define the type of viscous flow. For the primary phase, i.e. water, the viscosity of water is already predefined and taken as 0.001 kg/(m s) but for the secondary phase, i.e. iron ore particles, the exact calculation and representation of viscous effect is of utmost importance to get the most accurate results. Since the slurry behaves as Bingham plastic as seen in Part 1 studies of Mishra and Kaushal (2025), the model should be chosen as such to give inputs for yield stress and absolute viscosity. In that case, the Herschel-Bulkley model available in software, fits the best to provide input. Here, for simulating this, the Power-Law Index (n) is taken as 1 to treat it as a Bingham plastic model. Additionally, to consider the material's flow behavior under varying shear conditions, shear rate dependency has been considered. By using the Herschel-Bulkley model using the specified parameters, it is feasible to acquire more precise and dependable inputs for simulations, hence resulting in enhanced predictions for pressure drop across the pipeline.

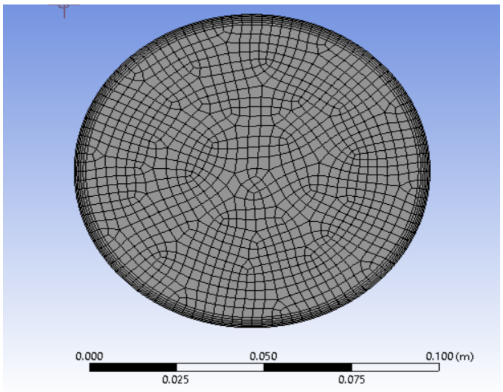

Fig. 1. Details of the mesh configuration within the cross-sectional profile of the pipeline.

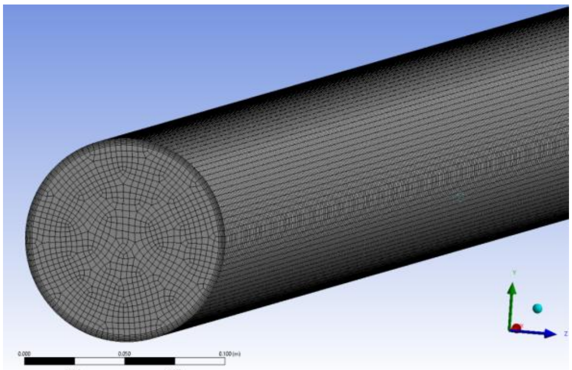

Fig. 2. Three-dimensional mesh details of the pipeline.

3 RESULTS AND DISCUSSION

3.1 Pressure drop analysis

During the current investigation, CFD simulations have been conducted utilizing the boundary conditions and mathematical models that were discussed in previous sections. The graphing of local solid concentration and the distribution of flow velocity takes place at the pipe outlet, while pressure drop is measured in the final segment of the pipeline. The pressure drop results were compared with those obtained in the experimental analysis in the Part I studies of Mishra and Kaushal (2024). Figure 3(a)–(e) shows the graphs for each efflux concentration with their experimental and data obtained from CFD-based model obtained. This analysis is also a follow-up study by Mishra and Kaushal (2023) to enhance the understanding of CFD-based models using Ansys fluent by taking more concentrations of iron ore including the additives range at different velocities.

The major variations in the experimental and simulated results are mostly seen at the lowest velocity and at the highest velocity. In general, there is a notable concurrence between the values computed through the 3D CFD-based model and the experimental results derived from the obtained graphs. The minimum velocity chosen for the simulation is 1 m/s. For 1 m/s of velocity, marginal variation in predicted pressure drop with respect to the experimental data is obtained for each efflux concentration. The maximum percentage deviation of predicted pressure drop with respect to the experimental result at 1.5 m/s of velocity is found to be 33.33 % at 65% efflux concentration. Further with the increase in additive range, the variation in the plot seems to reduce. The reason is that extremely tiny iron ore particles in the slurry flows used in the current study get equally distributed in the primary phase (water) at both very high concentrations and greater slurry velocities, increasing the primary phase's density. Deviations have been seen since the CFD model does not account for this element. Afterward, as the velocity increases the deviations in the pressure drop almost get equal to 0 and around 2–3 m/s of velocity, the CFD results coincide with the experimental results for pressure drop for all the efflux concentration cases showing the validity of the 3D CFD-based model. For the maximum additive range i.e. 1.0–1.5% w/w, there is a sharp deviation observed for all the cases after the velocity of 2.5 m/s. hence, this can be considered as the limitation of the computational model, as it is over-predicting the pressure drop.

3.1.1 Comparison of 3D CFD-based model with the proposed modified Slatter's Method

The predicted pressure drops utilizing the proposed modified Slatter approach in our previous studies and pressure drop predicted from 3D CFD–based model variations are depicted in Figure 4. Both the modified Slatter method and 3D CFD model accurately anticipate the pressure drop in the median velocity range. However, the modified Slatter technique predicts the pressure drop well within the minimum error range. Although more than 50% of the pressure drop data points fit into the ±15% error range, the 3D CFD-based model predicts well within the range of ±30%. Deviation of the rest of the points for pressure drop predicted using the 3D CFD–based model is mostly for higher velocity ranges and lower velocity as seen in Figure 4. This could be because fluent may not be able to resolve specific particles or the size distribution of the particles in the slurry since it assumes continuous flow. This restriction may have an impact on how accurately pressure drop predictions turn out, especially if the slurry has a large range of particle sizes that greatly alter flow resistance.

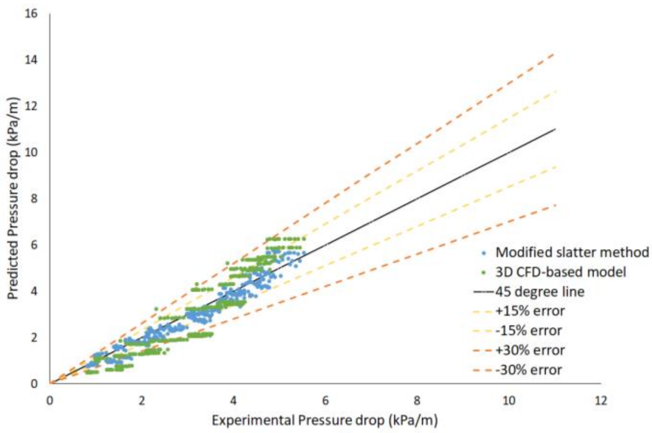

Fig. 4. Comparison of predicted pressure drop using proposed modified Slatter's method and 3D–CFD based model.

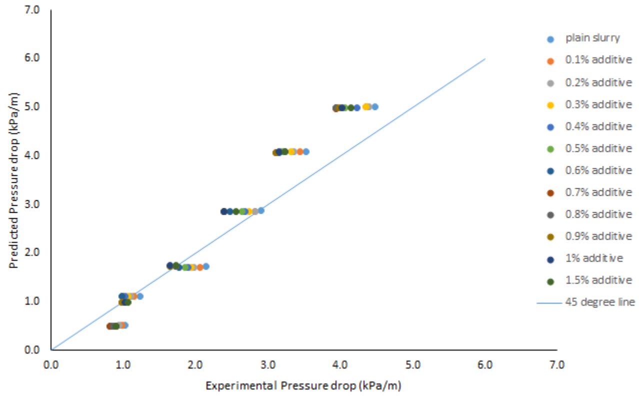

a) 60% w/w (Cvf= 22.02%) efflux concentration.

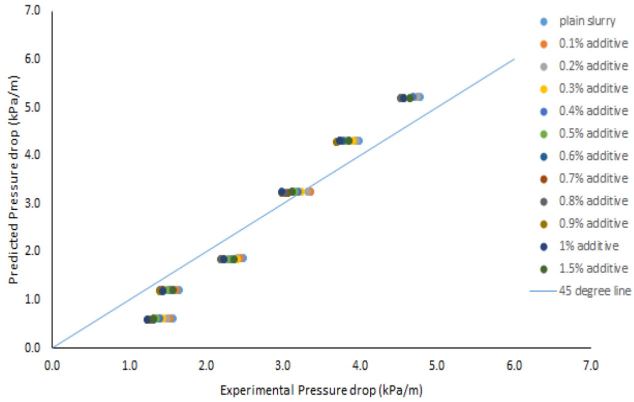

b) 65% w/w (Cvf= 25.90%) efflux concentration

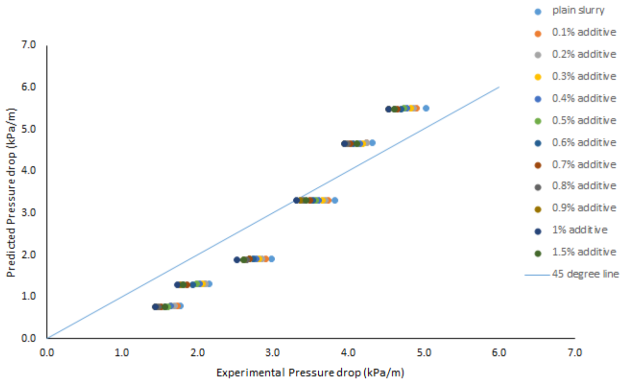

c) 68% w/w (Cvf= 28.50%) efflux concentration.

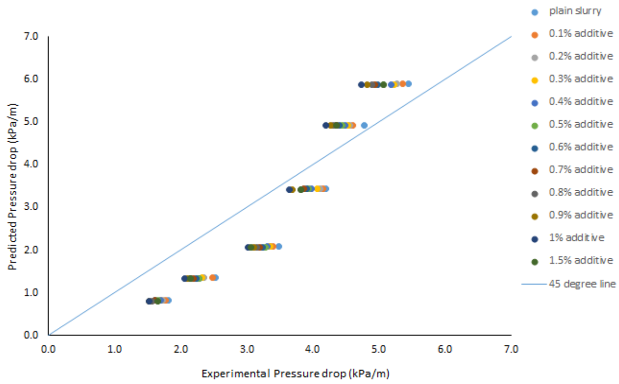

d) 70% w/w (Cvf= 30.50%) efflux concentration.

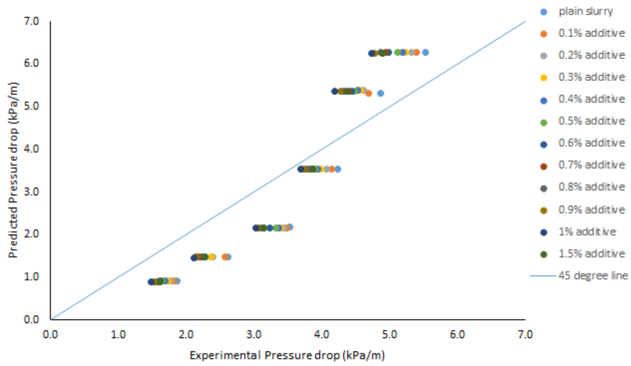

e) 72% w/w (Cvf= 32.70%) efflux concentration.

Fig. 3. Variation of Experimental pressure drop and Predicted pressure drop using 3D CFD–based model.

3.2 Velocity distribution

From Figure 5(a)–(e), velocity contours have been shown for a distance of 1 meter before the outlet to show the actual velocity variation inside the pipeline in its cross-sectional area. It can be seen that at the walls, the velocity of the slurry remains zero and it starts increasing while moving toward the center. It can be concluded that the solid particles travel at a much faster rate at the center pipeline's center for the different solid concentrations in all velocity ranges. Additionally, the contours of velocity are symmetric about the pipeline's mid-cross section (center) for all the shown mean velocities of flow. The interchange of momentum among the solid particles increases along with increases in velocity and solid concentration, which is why the velocity contours are symmetrical. The flow inside the pipeline becomes turbulent because of the interaction between solids and solid walls. Because of the viscous effect, solid particles along the pipe wall exhibit reduced velocity, whereas in the central region of the pipe, solid particles exhibit the highest velocity.

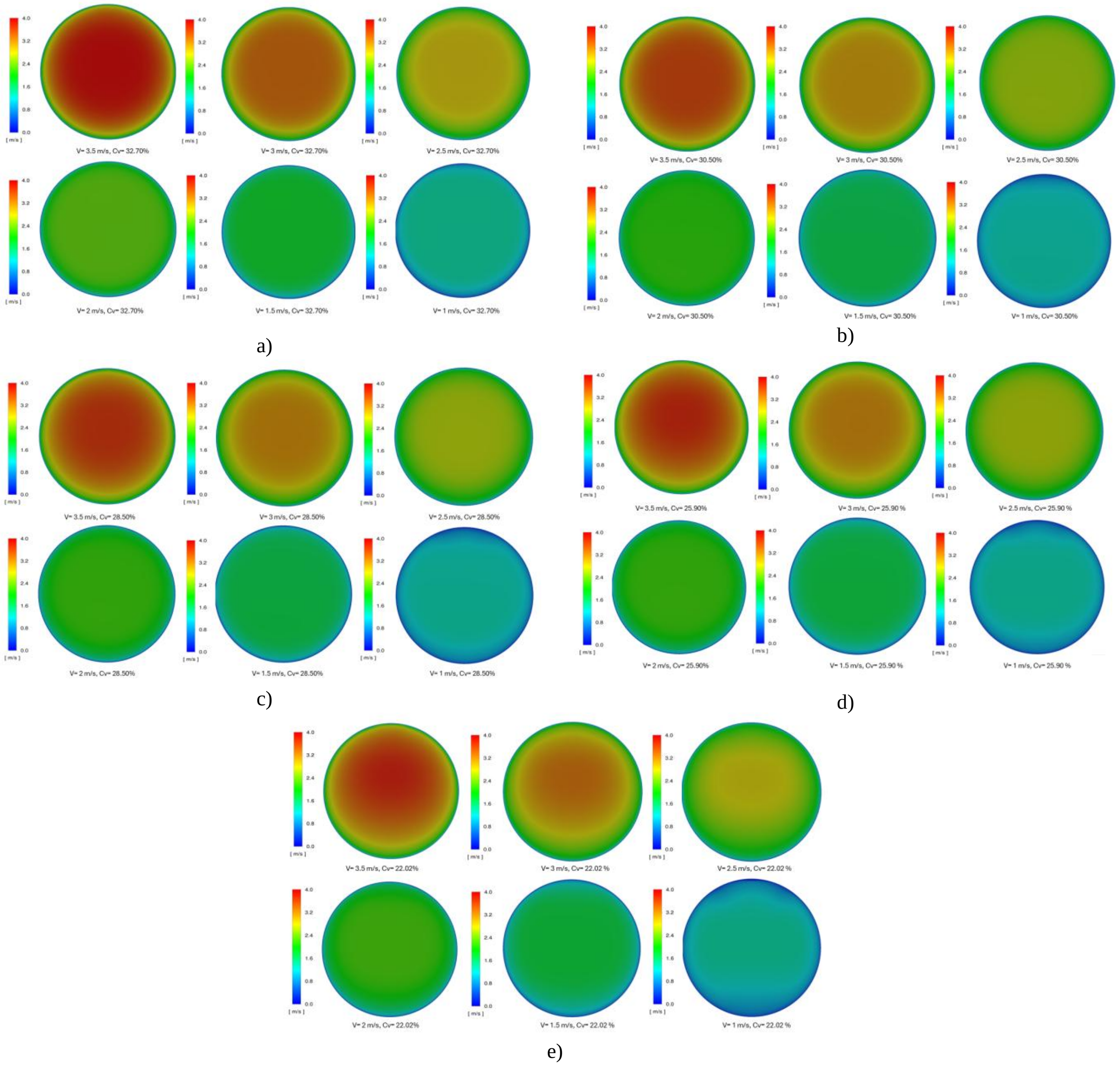

Fig. 5 (a)–(e). Velocity distribution profile at different efflux concentrations and different inlet velocities.

3.3 Slip velocity and vertical velocity distribution

Figure 6 and Figure 7 show the slip velocity variation along the longitudinal and transverse directions of the pipeline. The slip velocity is the difference between the mean particle velocity and the mean liquid velocity, which leads to the occurrence of a drag force. Considering the slip velocity along the longitudinal direction of the pipeline from the inlet to the outlet in Figure 6(a)–(e) (see appendices), it can be seen that the slip velocity first reduces to a maximum extent at the inlet and further stabilizes as the flow progresses to fully developed and moving towards the outlet. Three different additive ranges are taken, and their slip velocity is plotted in both Figure 6 and Figure 7 based on the results obtained in the above work for the optimum additive percentage from the rheological testing, and the maximum % additive range i.e., 1.5% for each case. Along the longitudinal axis, there is a marginal improvement in the slip velocity across all the optimum % additive ranges when compared with the plain slurry flow. This can be because the viscosity obtained is also much less for the optimum additive range which is taken as an input during the modelling.

In Figure 7(a)–(e) (see appendices), slip velocity along the transverse direction is taken at the mid-length of the pipeline for different additive ranges at different flow velocities. The figure also depicts the vertical velocity distribution in the pipeline when the additive range changes. It is observed that velocity is negative at the bottom section of the pipeline and stays in the negative range till it reaches the top of the pipeline as also seen in Kaushal et al (2012) for the slip velocity analysis. It can be because the particles in the bottom section of the pipe exhibit an inclination to travel in an upward direction. Vertical velocity distribution is shown in Figure 8(a)–(e) for iron ore. Particles in the top section of the pipe exhibit a downward motion because of gravitational force. The upward velocities of particles near the pipe wall cause the maximum concentration sites to move farther from the bottom of the pipe, as found experimentally at increasing concentrations and velocities. This phenomenon can be attributed to the high concentration of particles in the lower section of the pipe's cross-section, coupled with a negative slip velocity. This negative slip velocity indicates that energy is being transferred from the water to the particles. Consequently, this energy is then transferred to the upper section of the pipe, causing the particles to accelerate to a higher velocity than the water in the upper section.

Improvement in the slip velocity is also seen in all the cases at different additive ranges and extreme variation of slip velocity is not found for the optimum doses as compared to that of plain slurry. This improvement in the slip velocity ultimately leads to a more stable slurry flow in the pipeline. Hence, the addition of an additive (Sodium–Hexametaphosphate) makes the slurry less viscous and more stable.

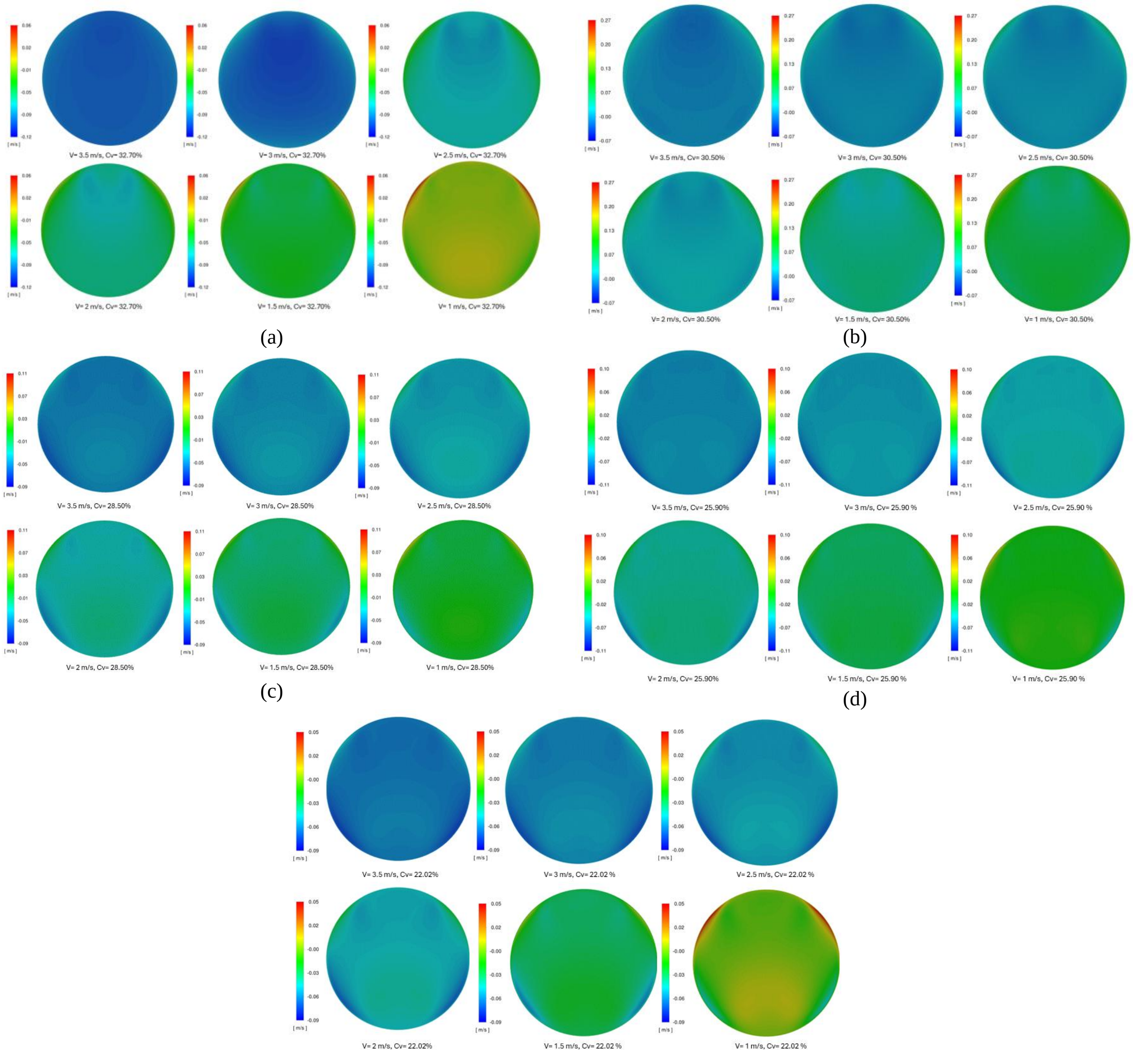

Fig. 8(a) – (e). Vertical velocity distribution profiles at different efflux concentrations and different inlet velocities.

3.4 Concentration profiles

In Figure 9(a)–(f), a solid concentration of iron ore slurry considering various efflux concentrations at the pipe outlet along with varied velocities is shown. For the highest concentration of slurry i.e., 72 % w/w (C_{vf} = 32.70%), the contours exhibit the highest concentration all over the cross section at every velocity. As the efflux concentration decreases the contours also exhibit very light mixing of the particles in the cross section. It is noted that the bottom portion of the pipe exhibits a modest deposition of solid particles for nearly all concentration profiles, which may be the result of the moving bed development. The heterogeneous flow regime is still present in the pipe's upper part.

3.5 Granular pressure and granular viscosity distribution

Figures 10 and 11 show the granular pressure Ps (x, y) and granular viscosity μs (x, y) at 3.5 m/s velocity with all the concentrations taken in the study. It can be seen in Figure 10 that the effect of granular pressure is restricted to the vicinity of the pipe-bottom zone at lower concentrations because fewer particles with lower turbulence intensities are moving there. Moreover, regarding the granular viscosity depicted in Figure 11, the highest value is observed at the pipe's bottom, with a slight impact noticeable up to the upper wall of the pipe.

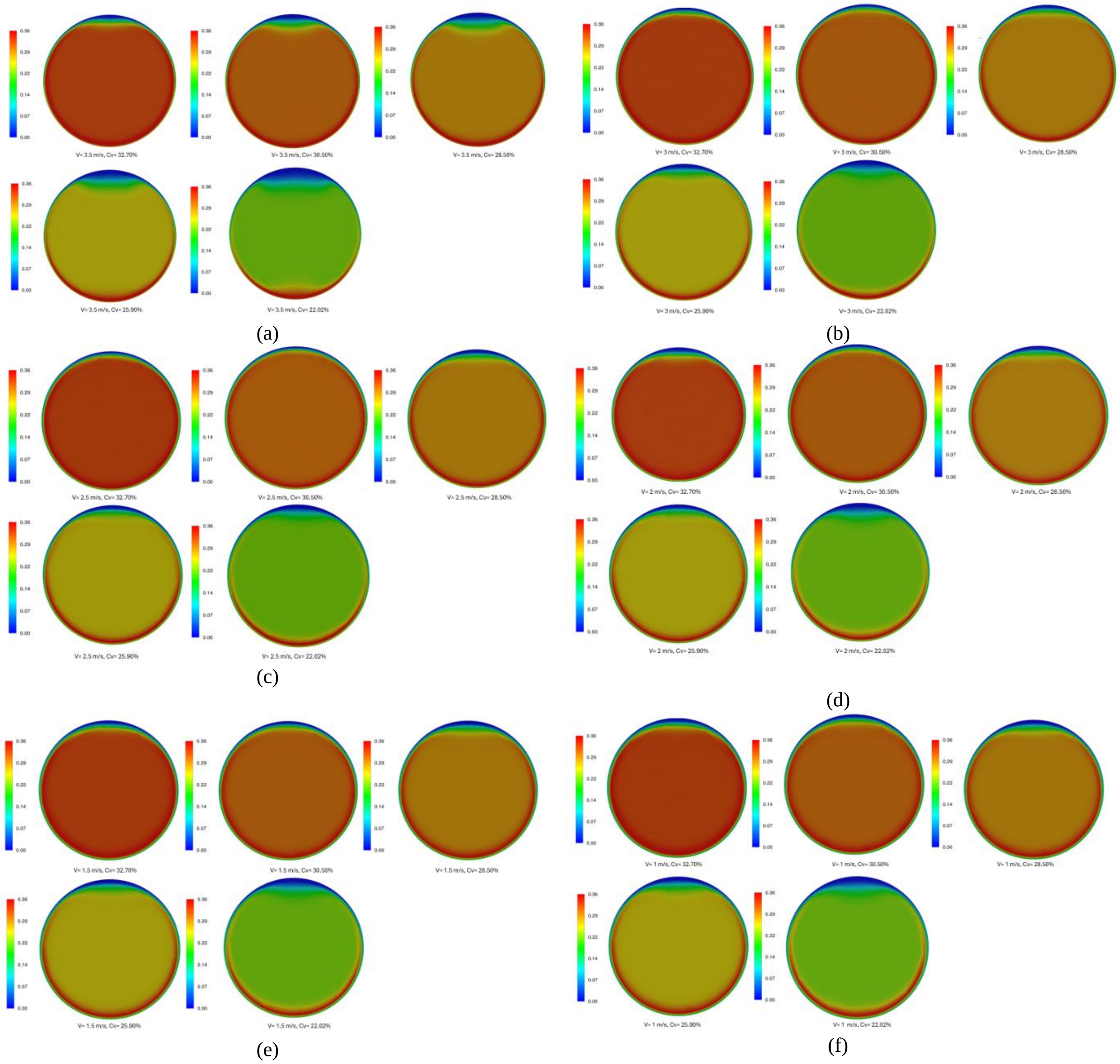

Fig. 9 (a) – (f). Solid Concentration profiles at the outlet of the pipeline considering varying velocities and efflux concentrations.

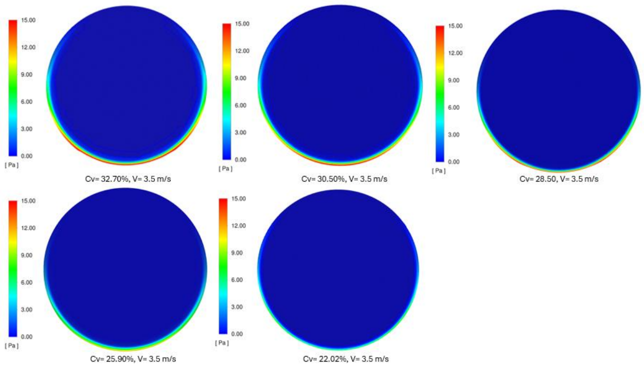

Fig. 10. Granular pressure Ps (x, y) due to particle interaction in Pascal at 3.5 m/s flow velocity.

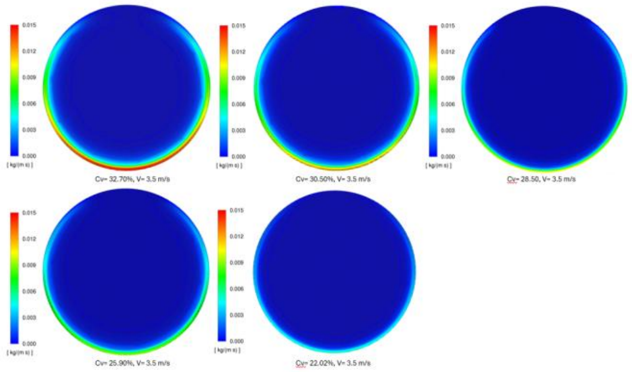

Fig. 11. Granular viscosity μs (x, y) in Pa s at 3.5 m/s flow velocity.

5 CONCLUSIONS

This paper has presented the computational analysis using a 3D CFD-based model for iron ore (55 µm mean diameter) slurry flows. A higher concentration (32.7% v/v – 22.02 % v/v) of slurry has been taken for a complete range of flow velocities (3.5 m/s – 1 m/s) without and with chemical additive (Sodium-hexametaphosphate). The following conclusions have been made from the study:

1. The Eulerian model has predicted the Pressure drop accurately with k-epsilon turbulence settings for all flow velocities.
2. The 3D CFD-based model is used for analyzing pressure drop in the slurry pipeline which predicts Pressure drop with almost zero error when compared with the experimental data obtained in Mishra & Kaushal (2024), for all efflux concentrations at velocities ranging from 2 m/s to 3 m/s. Further with the increase in additive range, the variation in the plot seems to reduce for the rest of the flow velocities.
3. The addition of the chemical additive also showed quite a good improvement in the slip velocity (both in the horizontal and vertical direction) for the optimum ranges, majorly due to the viscosity reduction. Hence, making the slurry flow more stable.
4. Solid particles are seen to exhibit reduced velocity near the walls in the velocity distribution contours due to the viscous effect, and the highest velocity is noted at the center. The concentration of the particles also seems to be higher at the bottom for a greater volume fraction of slurry as observed from the concentration profile, at all the flow velocities.
5. The granular pressure and granular viscosity increase with the increase in the concentration of slurry at the bottom of the pipeline.

The current study concludes that 3D CFD-based analysis proposed in the present study will help the designers to use the CFD model results for higher concentration for slurry conveyance to create a pipeline system for iron ore industries, thereby removing the necessity for time-consuming, costly, and labor-intensive experiments to be carried out on pilot plant loop test facilities.

Acknowledgements. The authors express gratitude to the Department of Civil Engineering, Indian Institute of Technology Delhi for providing the essential research facilities for this work.

RERENCES

Avksentiev, S.Y., Avksentieva, E.Y., 2017. Determining the parameters of the hydraulic transport of tailings for processing iron ore. In IOP Conference Series: Earth and Environmental Science, vol. 194, no. 3, p. 032003. IOP Publishing.

Das, S.N., Biswal, S.K., Mohapatra, R.K., 2020. Recent advances on stabilization and rheological behaviour of iron ore slurry for economic pipeline transportation. Materials Today: Proceedings, vol. 33, pp. 5093–5097.

Gidaspow, D., Bezburuah, R., Ding, J., 1992. Hydrodynamics of circulating fluidized beds: kinetic theory approach. Chemical Engineering Science, vol. 47, no. 8, pp. 2193–2211.

Hernández, F.H., Blanco, A.J., Rojas-Solórzano, L., 2008. CFD modeling of slurry flows in horizontal pipes. In Fluids Engineering Division Summer Meeting, vol. 48401, pp. 857–863.

Kaushal, D.R., Thinglas, T., Tomita, Y., Kuchii, S., Tsukamoto, H., 2012. CFD modeling for pipeline flow of fine particles at high concentration. International Journal of Multiphase Flow, vol. 43, pp. 85–100.

Kumar, N., Gopaliya, M.K., Kaushal, D.R., 2019. Experimental investigations and CFD modeling for flow of highly concentrated iron ore slurry through horizontal pipeline. Particulate Science and Technology, vol. 37, no. 2, pp. 232–250.

Kumar, N., Singh, D.B., Sharma, S.K., 2017. CFD analysis of two-phase flow characteristics in horizontal pipeline. International Journal of Advanced Research in Science and Engineering, vol. 7, no. 1, pp. 163–171.

Lun, C.K., Savage, S.B., Jeffrey, D.J., Chepurniy, N., 1984. Kinetic theories for granular flow: inelastic particles in Couette flow and slightly inelastic particles in a general flowfield. Journal of Fluid Mechanics, vol. 140, pp. 223–256.

Mishra, S.,Kaushal, D.R., 2023. Experimental and CFD analysis of iron ore slurry flow through pipelines at very high concentrations. In Proceedings of the TS20 Conference, September 2023. DOI:10.30825/4.14-18.2023.

Mishra, S., Kaushal, D.R., 2025. Highly concentrated iron ore slurry flow through pipeline with & without chemical additive; Part I: Experimental investigations and proposed model for the prediction of pressure drop. Journal of Hydrology and Hydromechanics.

Singh, R., Singh, J., Kumar, R., Gupta, M., 2024. Computational fluid dynamics of flow over a cylindrical tube for steady and transient flow conditions. International Journal on Interactive Design and Manufacturing (IJIDeM), pp. 1–11.

Received 20 August 2024
Accepted 8 March 2025

Appendices

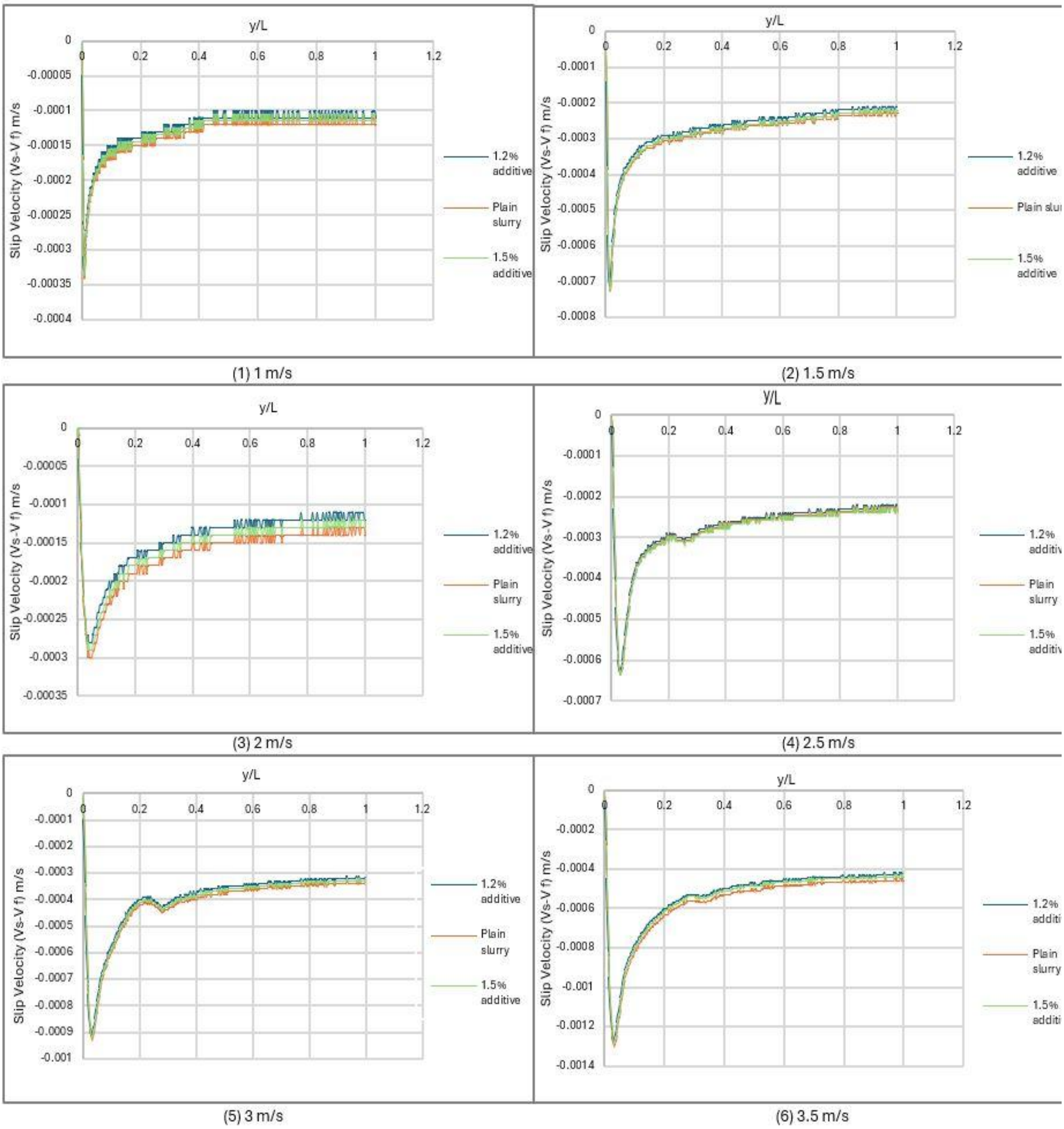

Fig. 6 (a). 3D CFD-based horizontal slip velocity profiles for different flow velocities at 72% w/w (Cvf= 32.70%) efflux concentration.

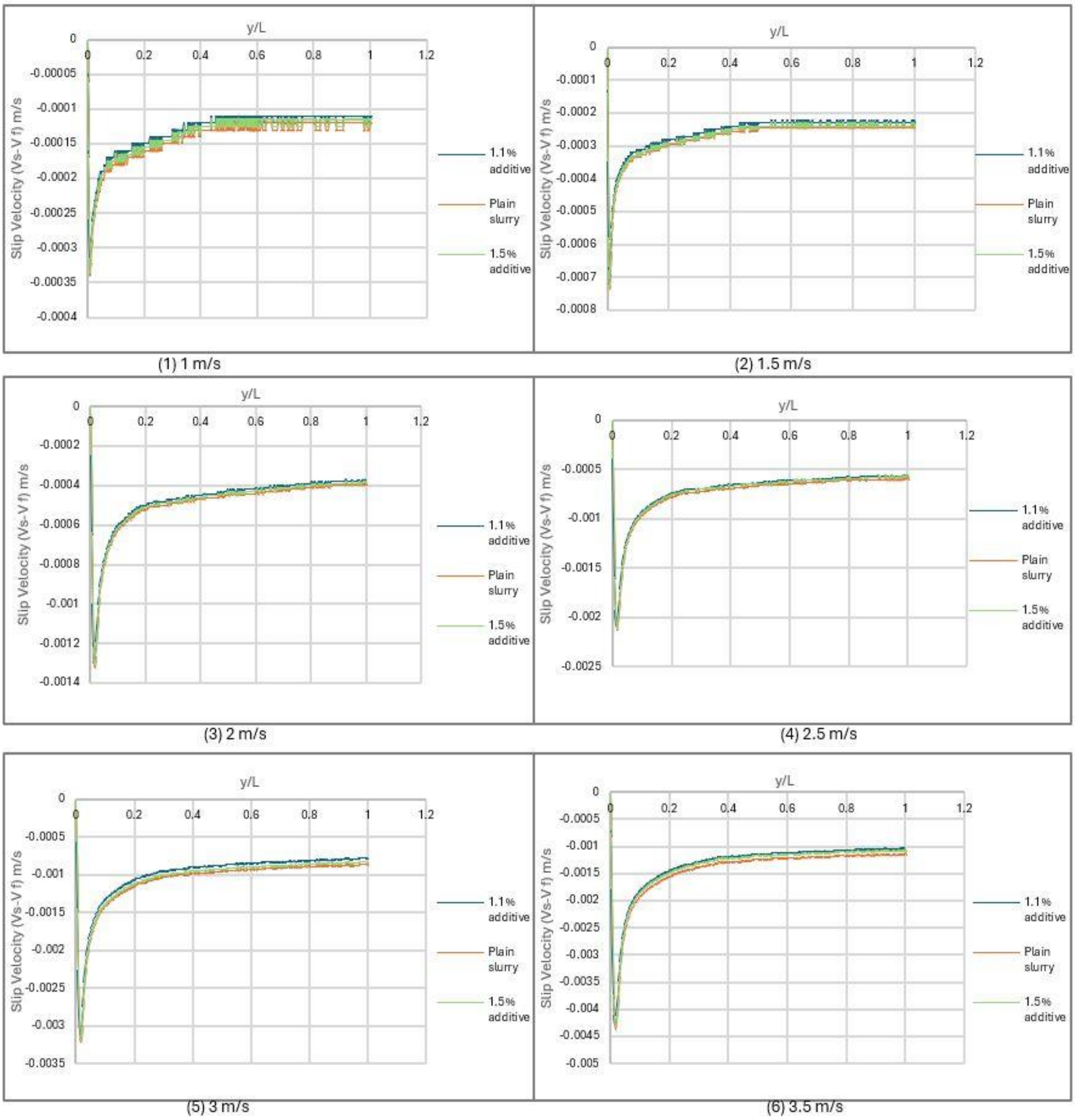

Fig. 6 (b). 3D CFD-based horizontal slip velocity profiles for different flow velocities at 70% w/w (Cvf= 30.50%) efflux concentration.

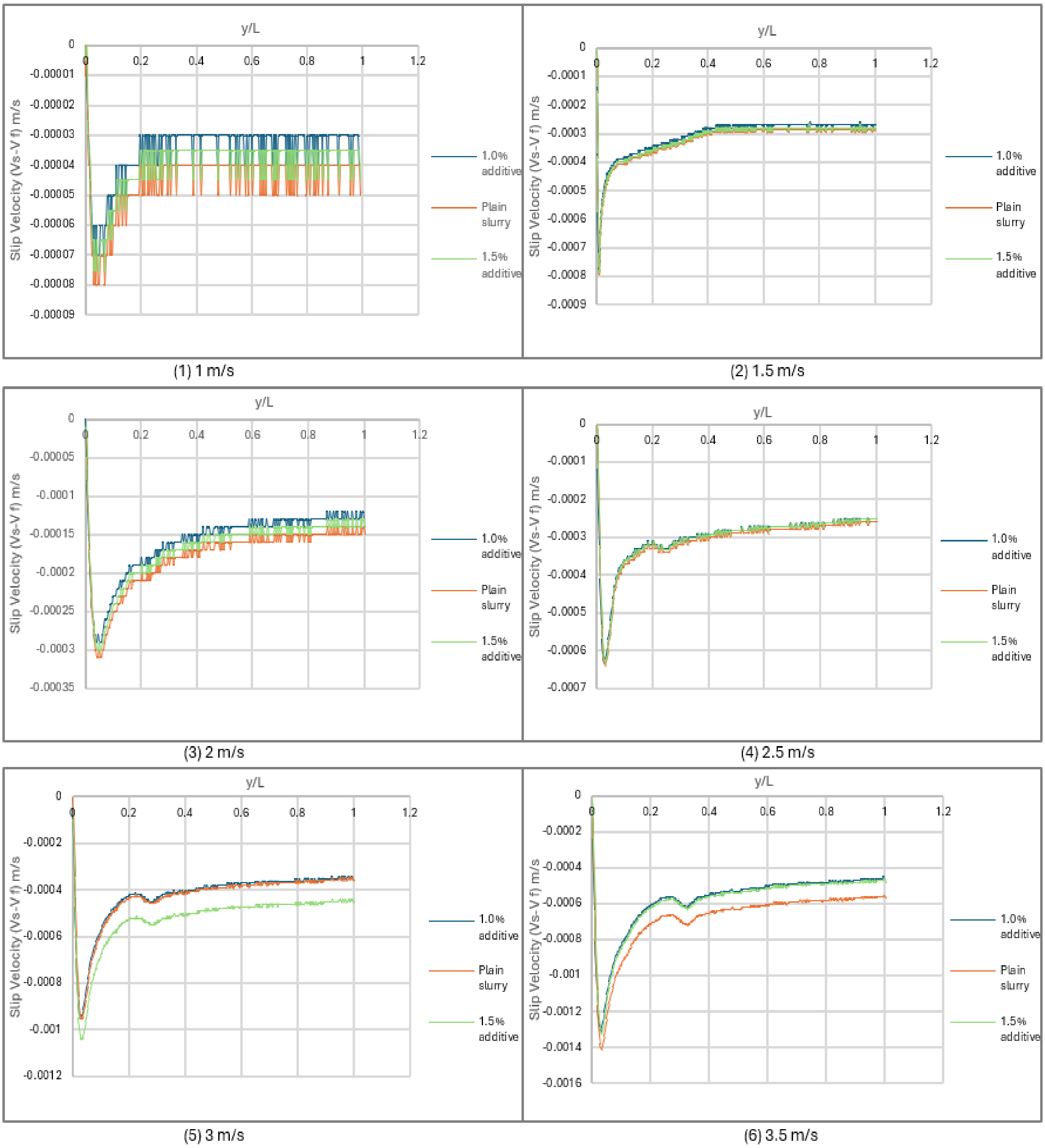

Fig. 6 (c). 3D CFD-based horizontal slip velocity profiles for different flow velocities at 68% w/w (Cvf= 28.50%) efflux concetration.

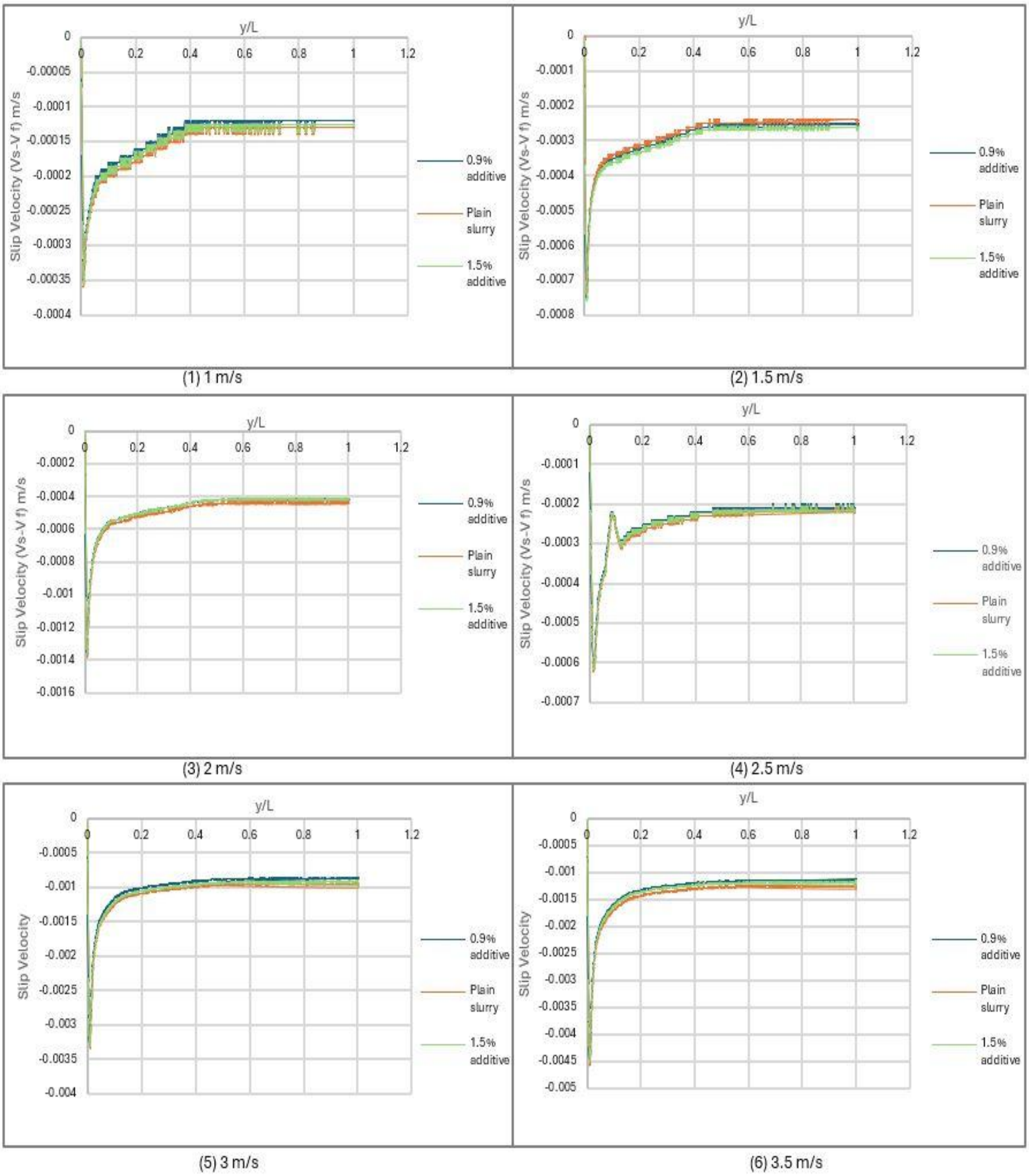

Fig.6 (d). 3D CFD-based horizontal slip velocity profiles for different flow velocities at 65% w/w (Cvf= 25.90%) efflux concentration.

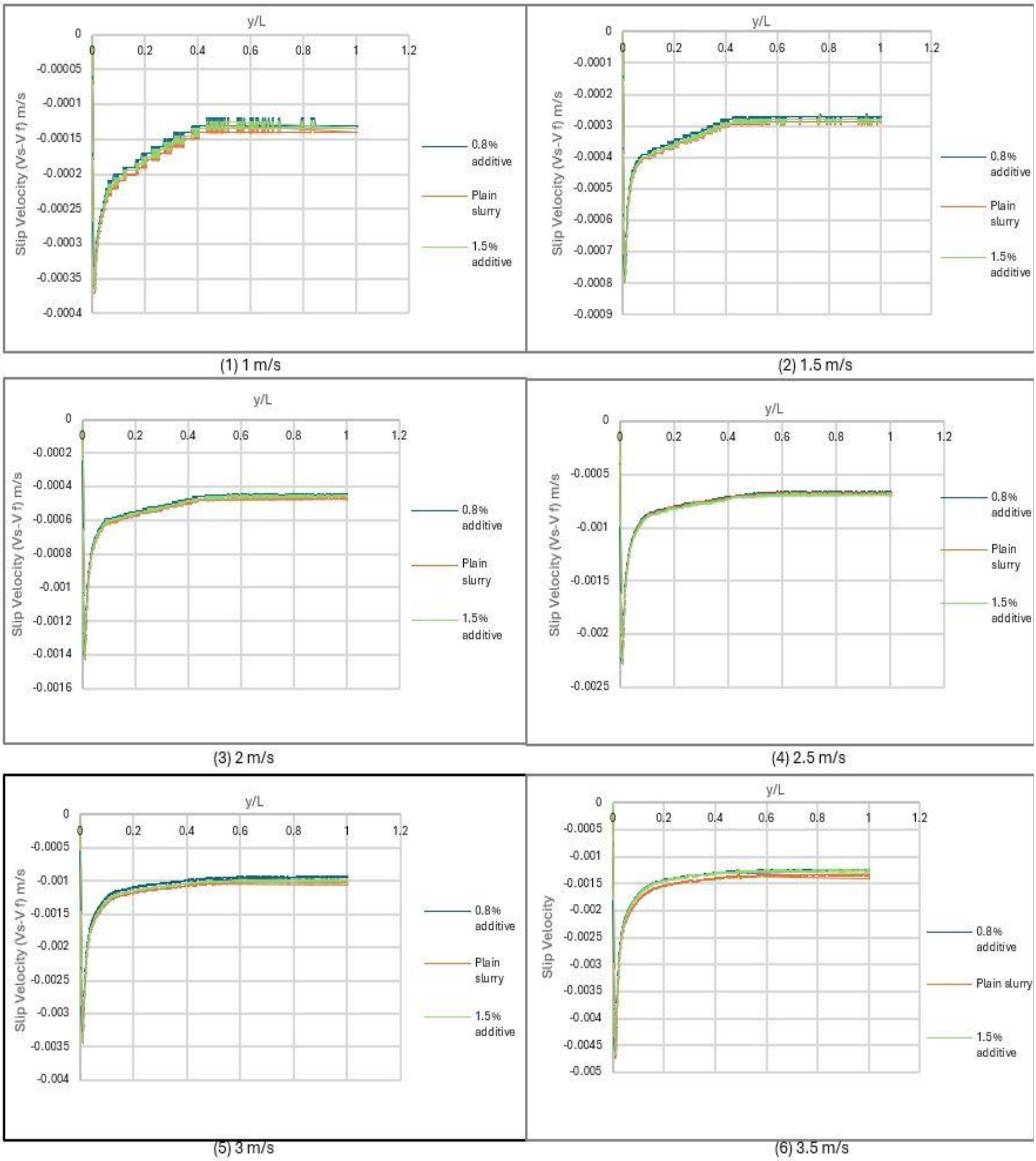

Fig. 6 (e). 3D CFD-based horizontal slip velocity profiles for different flow velocities at 60% w/w (Cvf= 22.02%) efflux concentration.

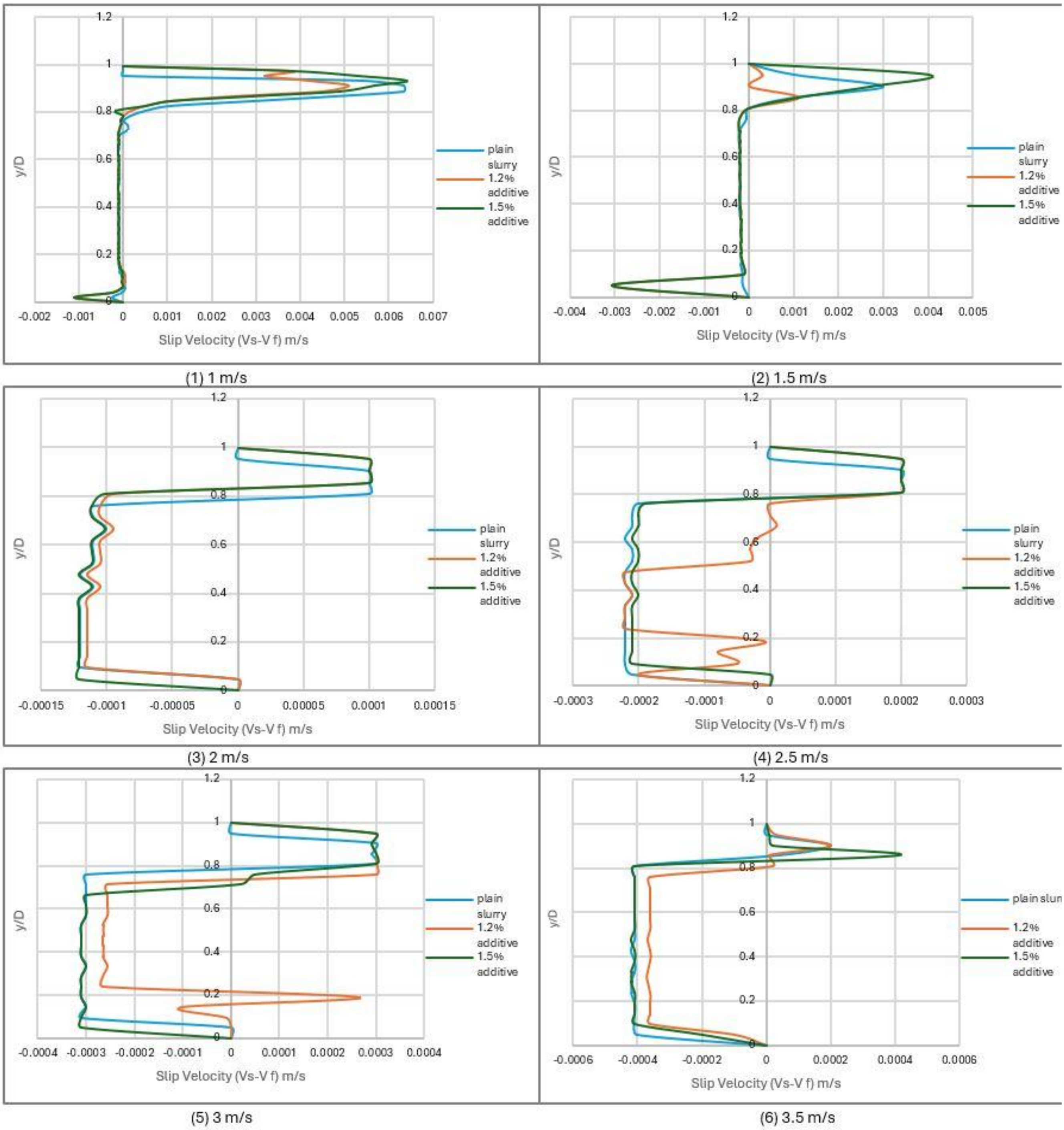

Fig. 7 (a). 3D CFD-based vertical slip velocity profiles for different flow velocities at 72% w/w (Cvf= 32.70%) efflux concentration.

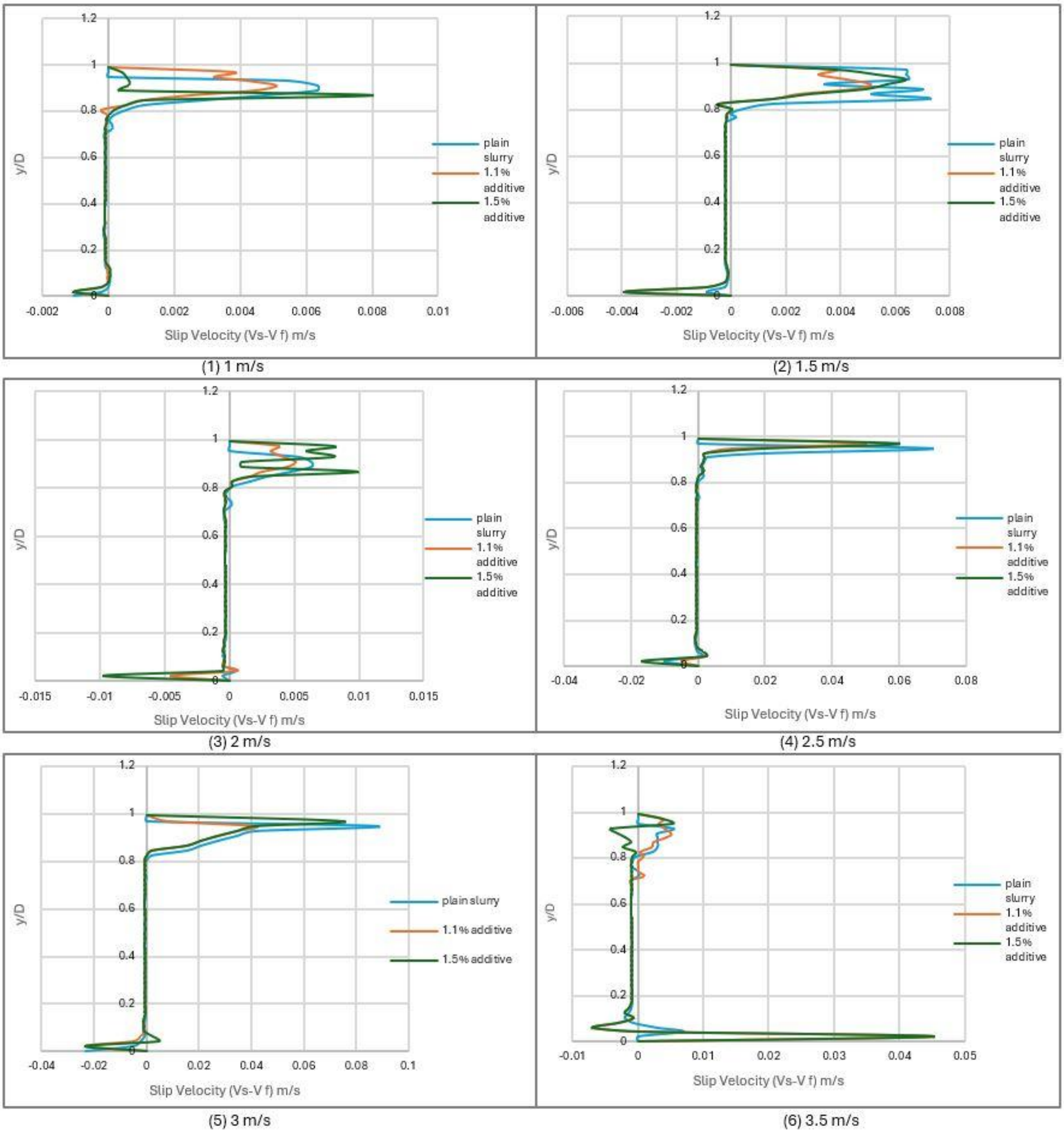

Fig. 7 (b). 3D CFD-based vertical slip velocity profiles for different flow velocities at 70% w/w (Cvf= 30.50%) efflux concentration.

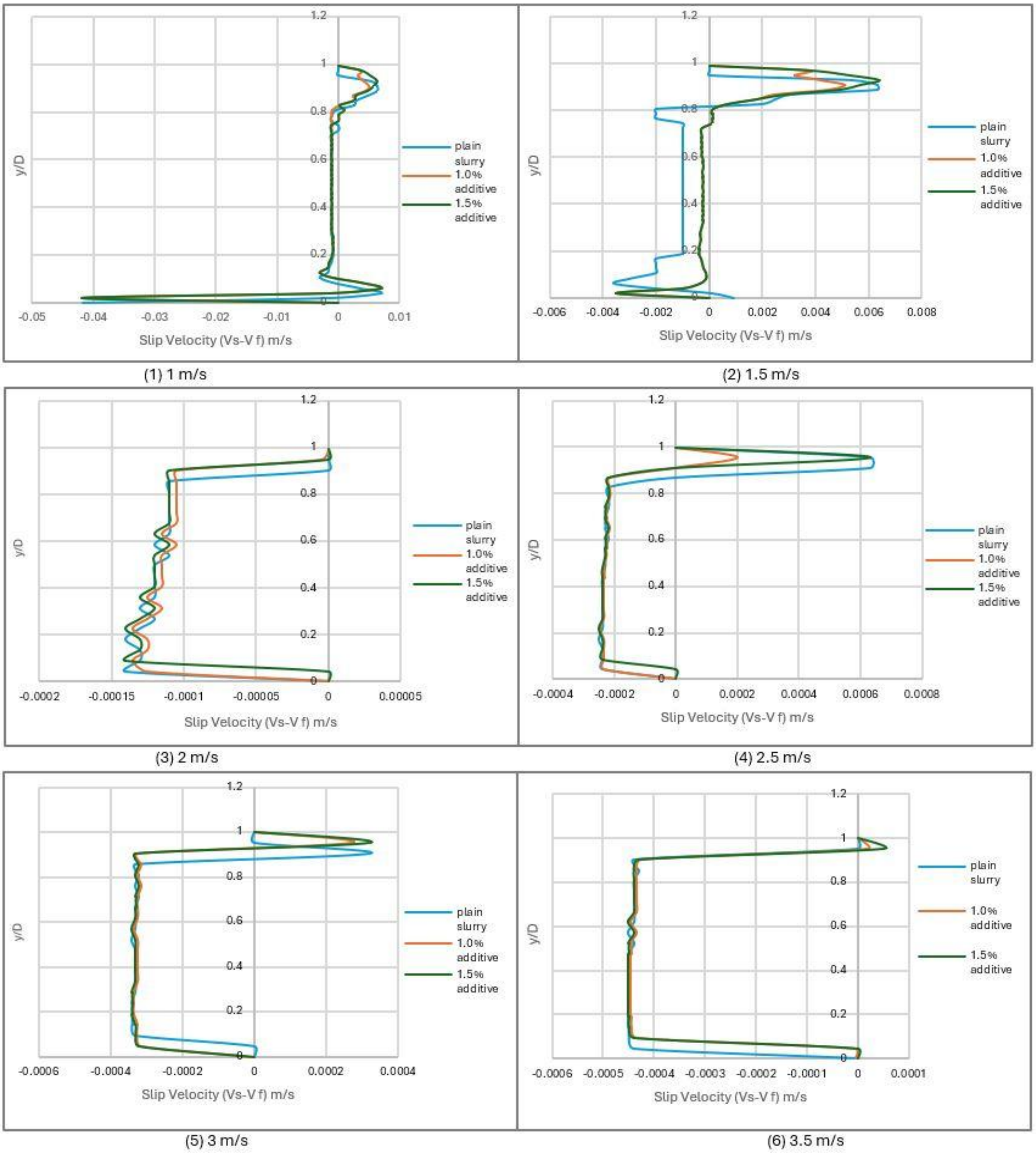

Fig. 7 (c). 3D CFD-based vertical slip velocity profiles for different flow velocities at 68% w/w (Cvf= 28.50%) efflux concentration.

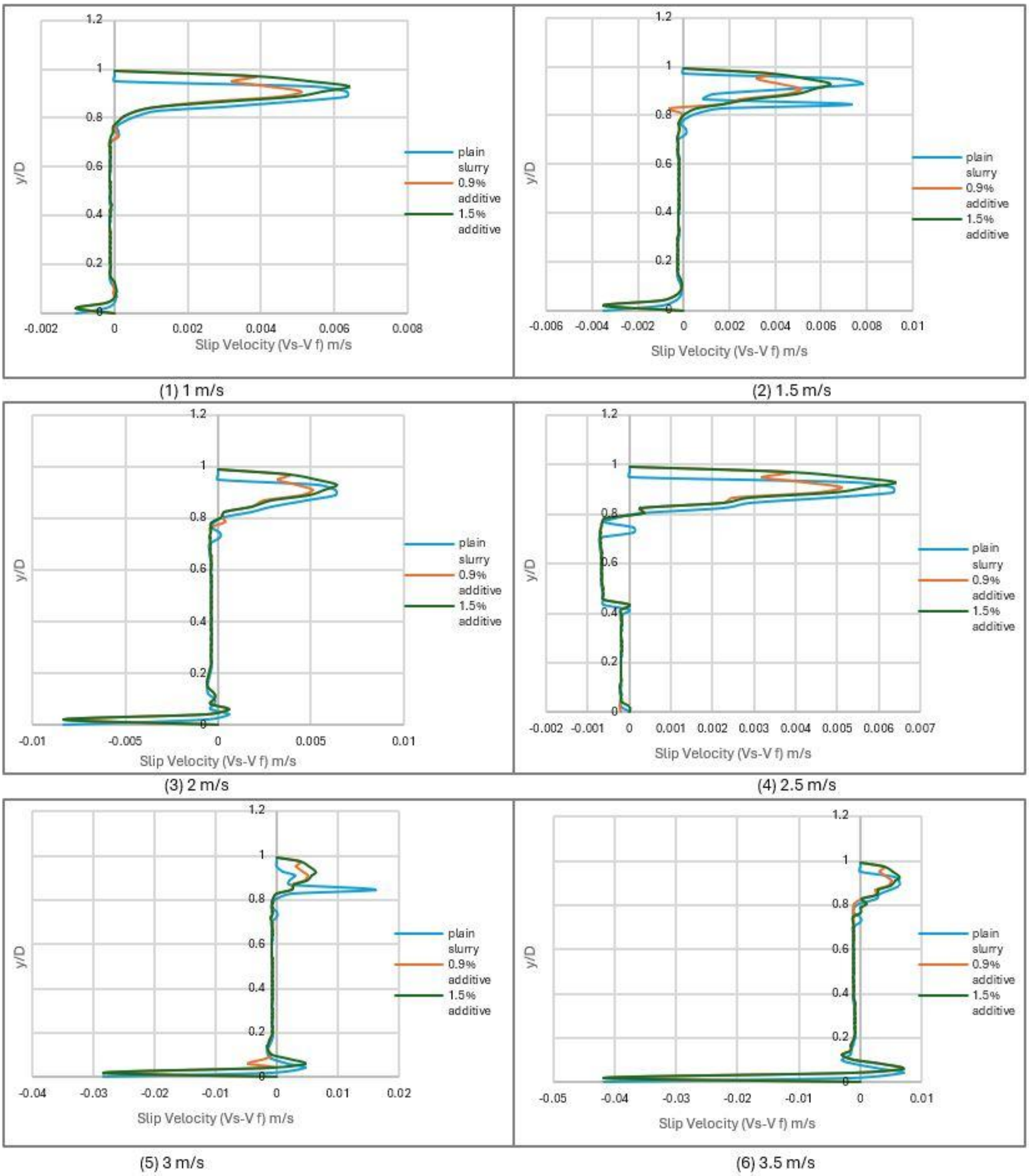

Fig. 7 (d). 3D CFD-based vertical slip velocity profiles for different flow velocities at 65% w/w (Cvf= 25.90%) efflux concentration.

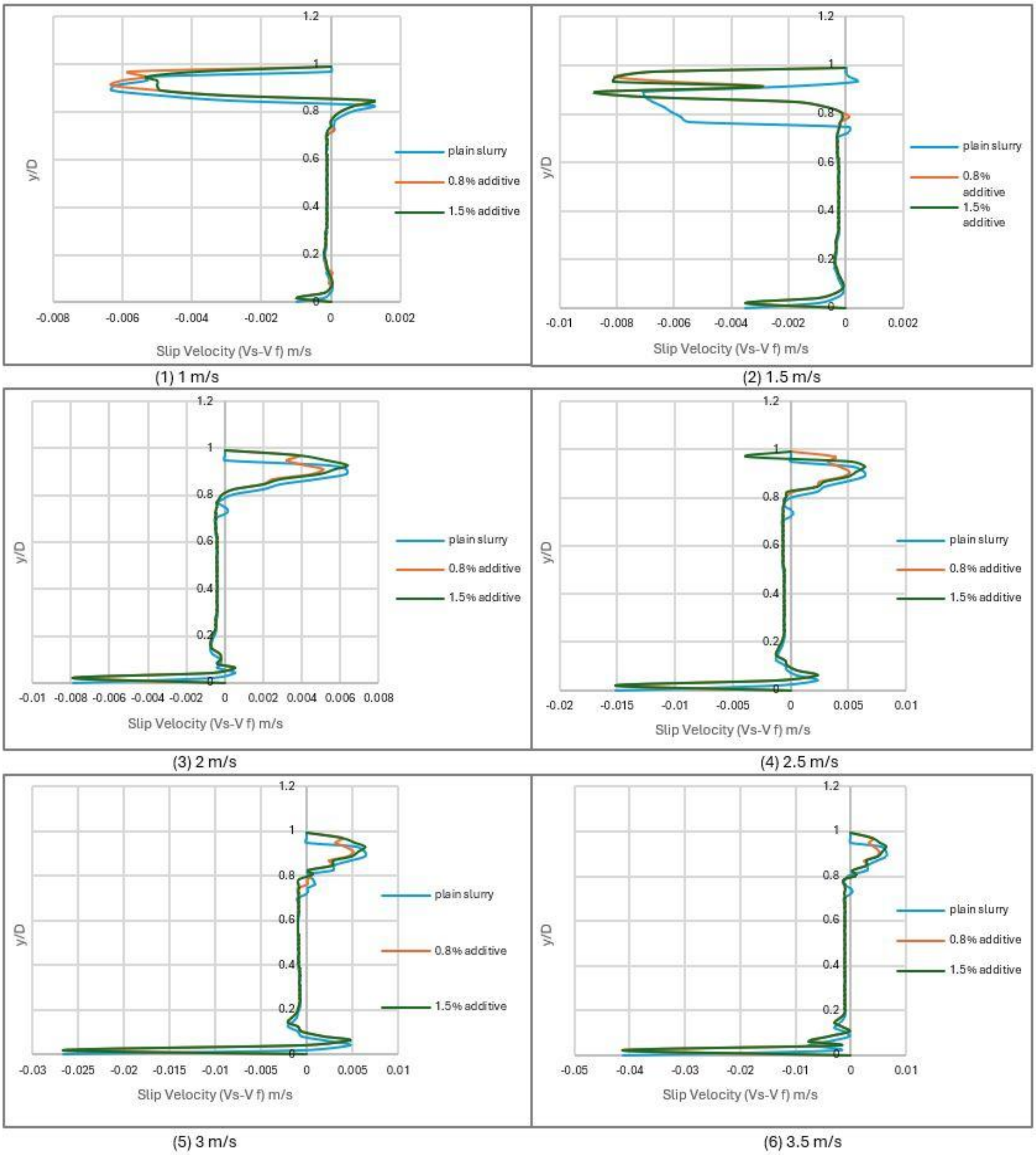

Fig. 7 (e). 3D CFD-based vertical slip velocity profiles for different flow velocities at 60% w/w (Cvf= 22.02%) efflux concentration.